Journal of Power, Energy, and Control

Research article

P-V Curve Tracing and CPF Validation for Static Voltage Stability Assessment Under Constant Power Factor Loading

Benjamin Egyin Wilson*, Emmanuel Agyepong Nyantakyi

Department of Electrical Engineering, University of Energy and Natural Resources, Sunyani, Ghana
*Correspondence: benjaminwilsonegyin@gmail.com

https://doi.org/10.62777/pec.v3i1.116

Received: 4 March 2026
Revised: 23 May 2026
Accepted: 7 June 2026
Published: 24 June 2026

Abstract: This paper presents an implementation-oriented methodology for static voltage stability assessment using P–V curve tracing, continuation power flow (CPF) validation, near-collapse voltage sensitivity analysis, and reactive capability diagnostics. Using the IEEE 30-bus benchmark system, the load at selected PQ buses is increased one bus at a time under a constant power factor (pf) growth model, and the resulting voltage magnitudes are recorded to form P–V curves. A two-stage step refinement strategy (coarse scan followed by fine steps near collapse) efficiently approximates the maximum solvable loading level and the corresponding critical voltage. To quantify vulnerability beyond loadability margin alone, a local slope-based sensitivity index, dV/dP, is computed from the tail of each curve. System-wide reactive power reserves and reactive limit hit/violation indicators are also extracted to characterize reactive support sufficiency and identify conditions where generator Q saturation would likely reduce practical margins. CPF is then applied to a subset of buses to benchmark the conventional tracing estimates and report PF-versus-CPF error statistics. The complete analysis is repeated for pf $\in$ {0.8, 0.9, 1.0} to quantify the impact of reactive demand coupling on voltage stability margins, curve steepness, and weak-bus ranking. A formal monotonicity theorem is established, proving that the loadability margin is nondecreasing in the load power factor under standard regularity conditions. The results demonstrate consistent identification of vulnerable buses, strong agreement between two-stage tracing and CPF nose points, and substantial margin improvement as pf approaches unity.

Keywords: Voltage stability, P-V curve, continuation power flow, loadability margin, reactive power reserve.

1. Introduction

Voltage stability is a fundamental security constraint in modern power systems because inadequate voltage support can trigger progressive voltage decline, load shedding, cascading outages, and in extreme cases, large-scale blackouts [1], [2], [3], [4], [5], [6]. Unlike transient stability, which is dominated by electromechanical dynamics and short-term rotor-angle behavior, voltage stability is primarily governed by the interaction between network reactive power balance, load characteristics, generator excitation

limits, and network transfer capability under both steady-state and dynamic conditions [1], [2], [3], [5], [7], [8]. Consequently, voltage stability assessment has become a core component of security-constrained operation and long-term grid reinforcement studies [6].

From an operational standpoint, voltage instability is commonly associated with the inability of the system to supply the reactive power demanded by loads and network losses as power transfers and loading levels increase [1], [3]. In stressed conditions, generators may reach reactive power capability limits, under-load tap changers (ULTCs) may respond by increasing reactive demand, and voltage-dependent loads may attempt to restore power consumption, thereby reinforcing the downward voltage trajectory [1], [4], [7]. These coupled mechanisms make voltage instability particularly challenging: the onset can be gradual and difficult to detect without dedicated assessment tools, yet the final collapse can occur abruptly once reactive reserves are exhausted [2], [3]. Motivated by industry experience, standardized definitions, assessment practices, and planning criteria have been established by IEEE working groups and other organizations [6]. The challenge is further amplified in inverter-dominated networks, where reduced synchronous-machine inertia and grid-forming converter dynamics directly affect voltage stability behaviour [9]. In parallel, synchrophasor-based monitoring and analytics have increasingly been used to support voltage stability and reactive power situational awareness in real-time operations.

A widely used static assessment approach is the construction of P–V (power–voltage) curves, which describe the relationship between bus voltage magnitude and a loading parameter (typically real power demand) under a specified loading direction [2], [5]. As loading increases, voltage typically decreases gradually at first and then more steeply near the stability boundary, producing the characteristic “nose curve” shape [2], [5]. The maximum loading point on the P–V curve corresponds (in theory) to a saddle-node bifurcation of the power flow equations, beyond which no equilibrium solution exists for the specified loading direction [2], [3], [10]. Practical implementations often approximate this boundary using conventional Newton power flow convergence behavior, identifying the last converged operating point as an empirical estimate of the critical loading level [5], [11]. However, conventional power flow can experience numerical difficulties near the nose point due to ill-conditioning of the Jacobian matrix, motivating the use of continuation methods for robust tracing and benchmarking [2], [3], [5], [12], [13].

Continuation power flow (CPF) was developed to robustly track solution branches of the power flow equations as a continuation parameter varies, thereby enabling stable traversal toward and beyond the region where Newton power flow becomes ill-conditioned [2], [3], [5]. CPF is typically implemented using predictor–corrector schemes with arc-length or related parameterization techniques to avoid singularities and maintain numerical stability [2], [5], [12]. Because CPF provides a theoretically grounded and numerically robust estimate of the stability boundary, it is frequently used as a benchmark to validate faster, approximate screening methods and sensitivity indices [3], [5]. In practice, system operators and planners may employ a combination of fast screening indices and targeted CPF studies to balance computational efficiency and accuracy [6].

In parallel with P–V analysis, a substantial body of research has focused on sensitivity indices and margin metrics that quantify proximity to voltage collapse. Classic examples include V–Q analysis, Jacobian-based indices, and modal analysis approaches that identify weak buses and critical modes of voltage instability [2], [3], [14], [15]. These

indices provide complementary insight: while loadability margins quantify "how far" the system can be stressed, sensitivity metrics quantify "how fast" voltage degrades in response to incremental loading and are often useful for ranking buses, identifying candidate locations for reactive compensation, and monitoring operating security [5], [16]. In particular, the local slope dV/dP near the stability boundary captures the steepness of the P–V curve and therefore serves as a practical proxy for voltage sensitivity under the selected loading direction [2], [5].

Reactive power limitations play a decisive role in voltage stability. Generator excitation systems have finite reactive capability boundaries, and when generators hit Qmin or Qmax, PV buses may effectively become PQ buses, altering the network voltage control structure and reducing voltage support [1], [4], [5]. This limit-induced change in bus type can significantly shrink stability margins relative to unconstrained analyses [2], [5], [17]. For this reason, many practical studies report not only loadability margins but also reactive reserves and diagnostics indicating whether the operating point violates or approaches reactive capability limits [6]. Moreover, power factor (pf) at load buses directly influences reactive demand: for constant pf growth, incremental reactive power scales with tan(arccos(pf)), implying that lower pf (more reactive demand) accelerates voltage decline and reduces margin [1], [3], [5], [7]. Thus, pf improvement and reactive compensation are common mitigation strategies in both distribution and transmission contexts [1], [6].

Beyond transmission planning, the need for transparent, reproducible voltage stability assessment workflows has increased due to the availability of open-source tools and standard test cases. MATPOWER has become a widely used research and education platform for power flow, optimal power flow, and continuation methods, supporting reproducible studies across IEEE benchmark systems [11]. Standardized test systems such as IEEE 30-bus allow controlled benchmarking of algorithms, comparison of metrics, and validation of approximate methods against more rigorous continuation analyses [18]. Public repositories such as the IEEE PES Power System Test Case Archive (PSTCA) have further supported consistent data-sharing and reproducible evaluation of stability algorithms across benchmark networks [18]. However, even in standardized contexts, methodological details matter: the selection of loading direction, step size strategy, power factor model, and the treatment of reactive limits can all affect the estimated stability margins and bus rankings [2], [4], [5]. Accurate characterization of network parameters, such as line and cable impedance, is also an upstream prerequisite for any voltage-stability study, and dedicated measurement methodologies have been developed in the broader power-system literature.

Motivated by these considerations, this paper develops and evaluates an implementation-oriented methodology for static voltage stability screening using P–V curve tracing across multiple PQ buses in the IEEE 30-bus system, with explicit power factor sweeps and complementary diagnostic metrics. In contrast to studies that rely exclusively on either conventional power flow or CPF, the proposed workflow combines a two-stage step refinement procedure, CPF validation, near-collapse sensitivity analysis, reactive capability diagnostics, and a formal monotonicity result linking power factor to loadability margin. We emphasize at the outset that the individual building blocks employed in this paper—P–V curve tracing, continuation power flow, generator-reactive diagnostics, and power-factor sensitivity studies—are well-established power-system tools rather than new algorithms. The primary value of the present work lies in (i) an integrated implementation-oriented workflow that combines these tools into a single reproducible MATPOWER-based pipeline, and (ii) a formal monotonicity theorem

(Theorem 1) that, to the best of the authors' knowledge, has not previously been stated in this form for the constant-power-factor loading model. This distinguishes the contribution from tutorial-style treatments of voltage stability on the IEEE 30-bus system [18]; the analytical Theorem 1 and its empirical verification across multiple power-factor scenarios are the principal additions, not the underlying numerical procedures. The contributions of this work are summarized below:

1) Multi-bus P–V curve tracing with step refinement: An implementation-oriented framework is developed to generate P–V curves for multiple PQ load buses in the IEEE 30-bus system using a two-stage (coarse-to-fine) loading strategy. The two-stage refinement is used here as a practical efficiency choice rather than as an algorithmic contribution; sub-percent agreement with continuation power flow on a well-behaved benchmark is an expected outcome that serves as a sanity check on the pipeline, not as a novel performance claim. The complete tracing procedure is formalized as Algorithm 1.
2) Loadability margin and critical voltage extraction for weak-bus ranking: For each stressed bus and power factor scenario, the method extracts the last-converged critical voltage V_{cr} and the real-power loadability margin $Margin = P_{max} - P_{D0}$. Building on prior work that has identified weak and critical buses through related diagnostics in test systems, the ranking combines the present loadability-margin diagnostic with the near-collapse sensitivity index of Contribution 4 below.
3) Monotonicity of loadability margin with respect to power factor: A formal theorem (Theorem 1) is established proving that the loadability margin is nondecreasing in the power factor pf under standard regularity conditions.
4) Near-collapse voltage sensitivity metric: A practical sensitivity index based on the local slope of the P–V curve, dV/dP, is computed using a least-squares fit on the final segment of the curve.
5) Reactive capability diagnostics without destabilizing conventional tracing: System-level reactive power reserves and reactive limit hit/violation indicators are computed from converged solutions.
6) CPF-based validation and error quantification: Continuation power flow (CPF) is executed for a subset of buses to benchmark the conventional tracing estimate of the stability boundary.
7) Power factor sweep for comparative stability assessment: The complete workflow is repeated for pf $\in$ {0.8, 0.9, 1.0}, providing a structured quantification of how reactive demand coupling affects P–V curve shape, stability margins, sensitivity indices, and reactive stress indicators across buses.

The remainder of this paper is organized as follows. Section 2 presents the problem formulation and preliminaries. Section 3 describes the study design and evaluation framework. Section 4 details the methodology. Section 5 presents the numerical results. Section 6 concludes the paper and outlines future extensions.

2. Problem Formulation and Preliminaries

This section introduces the modeling assumptions, notation, and performance metrics used throughout the paper.

2.1. Network Model and Notation

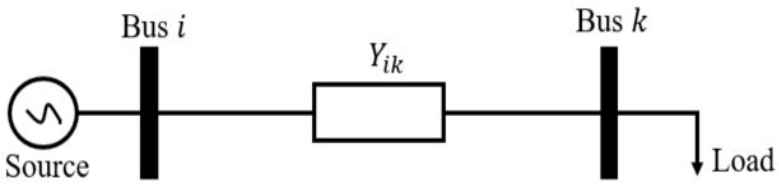

Figure 1. Single-line diagram of a simple electrical power system.

Consider an N-bus power system (Figure 1) represented by the complex bus admittance matrix:

$$Y_{bus} = G + jB \tag{1}$$

where *G* and *B* are the conductance and susceptance matrices, respectively. Let the complex bus voltage phasor at bus *i* be:

$$\tilde{V}_i = V_i e^{j\theta_i} \tag{2}$$

where V_i is the voltage magnitude and θ_i is the voltage angle. The complex power injection at bus *i* is:

$$\tilde{S}_i = P_i + jQ_i \tag{3}$$

where P_i and Q_i denote the net real and reactive power injections (generation minus demand). The current injection is:

$$\tilde{I}_i = \sum_{k=1}^{N} Y_{ik}\tilde{V}_k \tag{4}$$

and the power flow relationship at bus *i* satisfies described as:

$$\tilde{S}_i = \tilde{V}_i \tilde{I}_i^* \tag{5}$$

where $(\cdot)^*$ denotes complex conjugate. Throughout this paper, buses are categorized as slack/reference (REF), generator-controlled voltage (PV), and load (PQ) buses following standard power flow conventions.

2.2. Power Flow Equations

The AC power flow equations can be written in polar form by separating real and reactive power balances at each bus. For bus *i*, the balance equations are:

$$P_i = V_i \sum_{k=1}^{N} V_k (G_{ik}\cos(\theta_i - \theta_k) + B_{ik}\sin(\theta_i - \theta_k)) \tag{6}$$

$$Q_i = V_i \sum_{k=1}^{N} V_k (G_{ik}\sin(\theta_i - \theta_k) - B_{ik}\cos(\theta_i - \theta_k)) \tag{7}$$

Let $x = [\theta^T\ V^T]^T$ denote the vector of unknown voltage angles and magnitudes. The power flow problem is a nonlinear system.

$$F(x) = 0 \tag{8}$$

This typically solved using Newton-based methods. The Jacobian matrix $J = \partial F/\partial x$ becomes ill-conditioned as the operating point approaches a saddle-node bifurcation associated with voltage collapse.

2.3. Load Stressing Direction and Constant Power Factor Growth

Voltage stability margins depend on the loading direction. In this work, a bus-by-bus stressing direction is adopted. Let bus *b* be the stressed *PQ* load bus, with base-case demand ($P_{D0,b}$, $Q_{D0,b}$). For a real power increment $\Delta P \geq 0$, the constant power factor (pf) stressing model is:

$$P_{D,b}(\Delta P) = P_{D0,b} + \Delta P \tag{9}$$

$$Q_{D,b}(\Delta P) = Q_{D0,b} + \tan(\arccos(\mathrm{pf}))\,\Delta P \tag{10}$$

where $pf \in (0, 1)$ is the prescribed lagging power factor, and

$$k_{pf} \triangleq tan(arccos(pf)) \tag{11}$$

directly controls the rate at which reactive demand increases with real demand. As $pf \to 1$, $k_{pf} \to 0$ and incremental loading becomes nearly purely real-power-driven.

2.4. Definition of P–V Curve and Loadability Margin

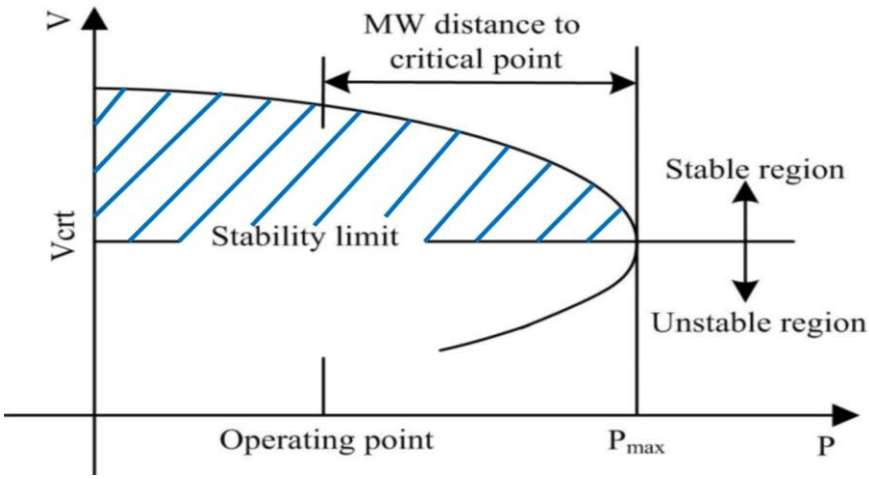

Figure 2. P–V curve and loadability margin.

As shown in Figure 2, the P–V curve is the set of operating points obtained by solving the power flow equations as ΔP increases, and recording the pair ($P_{D,b}(\Delta P)$, $V_b(\Delta P)$). Under the adopted stressing model, the P–V curve is represented as:

$$\mathcal{C}_{\mathrm{b}} \triangleq \left\{\left(\mathrm{P_{D,b}}(\Delta \mathrm{P}), \mathrm{V_b}(\Delta \mathrm{P})\right) : \Delta \mathrm{P} \in \left[0, \Delta \mathrm{P_{max,b}}\right]\right\} \tag{12}$$

The loadability margin is defined as:

$$\mathrm{Margin}_b \triangleq P_{max,b} - P_{D0,b} \tag{13}$$

Buses with smaller $Margin_b$ are considered more vulnerable to local demand growth in the studied direction.

2.5. Near-Collapse Voltage Sensitivity Metric

While margin quantifies the distance to the boundary, it does not fully capture how rapidly voltage degrades near collapse. Therefore, a slope-based sensitivity index is employed using the tail segment of the P–V curve:

$$V \approx aP + c \tag{14}$$

$$\left.\frac{dV}{dP}\right|_{near\ collapse} \approx a \tag{15}$$

A more negative a (larger $|a|$) indicates higher sensitivity and a steeper voltage drop for incremental loading near the stability limit.

2.6. Reactive Power Capability Diagnostics

Reactive power availability is central to voltage stability. The system-wide upward and downward reactive reserves are defined as:

$$Q_{res,up} \triangleq \sum_{g} max(0, Q_{g,max} - Q_g) \tag{16}$$

$$Q_{res,dn} \triangleq \sum_{g} max(0, Q_g - Q_{g,min}) \tag{17}$$

In addition, limit proximity and violation counters are computed:

$$\#Q_{hits} \triangleq \sum_{g} 1\left(|Q_g - Q_{g,max}| \le \varepsilon \text{ or } |Q_g - Q_{g,min}| \le \varepsilon\right) \tag{18}$$

$$\#Q_{viol} \triangleq \sum_{g} 1\left(Q_g > Q_{g,max} + \varepsilon \text{ or } Q_g < Q_{g,min} - \varepsilon\right) \tag{19}$$

2.7. CPF-Based Validation Metrics

To benchmark the conventional tracing estimate, CPF is used to obtain a more robust approximation of the nose point. The agreement is quantified using:

$$AbsErr_b \triangleq |P_{max,b} - P_{nose,b}| \tag{20}$$

$$RelErr_b(\%) \triangleq 100 \frac{AbsErr_b}{|P_{nose,b}|} \tag{21}$$

3. Study Design and Evaluation Metrics

This section specifies the study cases, bus selection, parameter settings, and evaluation criteria used to ensure a consistent and reproducible comparison across buses and power factor scenarios. To quantify the influence of reactive demand coupling on voltage stability, three load power factor scenarios are evaluated: $pf \in \{0.8, 0.9, 1.0\}$. The $pf = 1.0$ case serves as a reference condition. The $pf = 0.8$ case represents a high reactive-demand condition.

The analysis focuses on the following PQ buses in the IEEE 30-bus system: $B = \{7, 8, 9, 11, 14, 16, 17, 18, 19, 20, 26\}$. A bus-by-bus stressing strategy is used. Each bus produces one P–V curve per pf scenario. A two-stage step-size configuration is adopted. The coarse increment ΔP_{coarse} (e.g., 1 MW) provides rapid approach to the solvability boundary, and the fine increment ΔP_{fine} (e.g., 0.1 MW) provides refined estimation. The tracing process stops at the first nonconvergent step. For each bus b and power factor scenario, the following metrics are reported: the critical voltage $V_{cr,b}$, the loadability margin $Margin_b$, the near-collapse slope dV/dP, and the reactive reserve and limit counters $Q_{res,up}$, $Q_{res,dn}$, $\#Q_{hits}$, and $\#Q_{viol}$. CPF is used as a benchmark for a subset of buses: $B_{CPF} = \{7, 11, 14, 18, 26\}$. For each bus and pf scenario, CPF is executed along the same loading direction as the conventional tracing procedure.

4. Methodology

This section describes the methodology used to assess static voltage stability in the IEEE 30-bus benchmark network via P–V curve tracing, CPF validation, a near-collapse voltage sensitivity index *dV/dP*, and reactive power margin diagnostics. The workflow is implemented in MATLAB using MATPOWER v8.1.

4.1. Test System and Software Environment

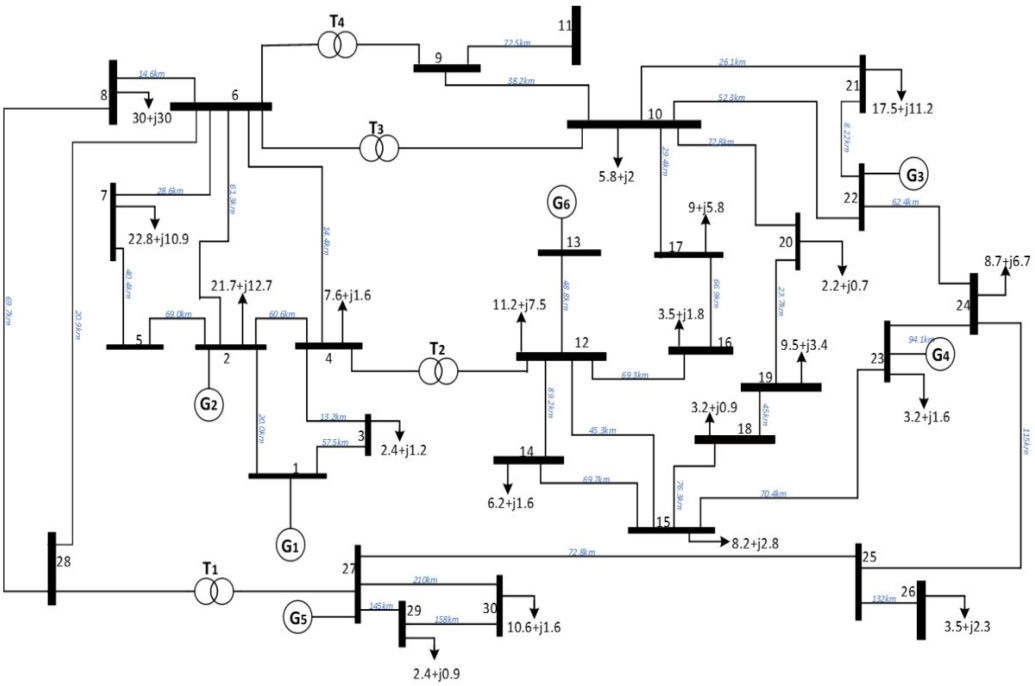

Figure 3. IEEE 30-bus test system.

All studies are performed on the IEEE 30-bus test system (Figure 3) provided in MATPOWER as case30. The network is assumed balanced and operates under steady-state sinusoidal conditions. The MATPOWER routines *loadcase*, *runpf*, and *runcpf* are used for the base power flow, conventional power-flow-based P–V tracing, and continuation power flow validation, respectively.

At each loading step, the system operating point is obtained by solving the nonlinear AC power flow equations (6)–(7). MATPOWER computes the solution via Newton's method and returns a convergence flag. The P–V curve is assembled from all successful points, and the tracing process terminates at the first nonconvergent step. While a loss of convergence is not identical to the theoretical saddle-node bifurcation location, it is a widely used practical indicator of proximity to the voltage collapse boundary. The constant power factor stressing model from Section 2.3 is adopted. The methodology evaluates $pf \in \{0.8, 0.9, 1.0\}$. For $pf = 1.0$, $k_{pf} = 0$ and incremental reactive demand is zero.

4.2. P–V Curve Tracing With Two-Stage Step Refinement

A two-stage step size strategy is used. Stage 1 (coarse scan) increases ΔP using a coarse step to rapidly approach the solvability boundary. Stage 2 (fine refinement) backs off by one coarse step and continues with a smaller step to refine the estimate. The complete procedure is formalized in Algorithm 1.

Algorithm 1. Two-stage P-V curve tracing.

Require: Bus index b, power factor pf, coarse step ΔPc, fine step ΔPf, base case data mpc
Ensure: P–V curve Cb, critical point (Pmax,b, Vcr,b)

```
kpf ← tan(arccos(pf))
Load base case; store (PD0,b, QD0,b)
ΔP ← 0; Cb ← ∅
Solve base power flow; record (PD0,b, Vb)
Cb ← Cb ∪ {(PD0,b, Vb)}
— Stage 1: Coarse Scan —
ΔPlast ← 0;  converged ← true
while converged do
    ΔP ← ΔP + ΔPc
    PD,b ← PD0,b + ΔP
    QD,b ← QD0,b + kpf · ΔP
    Update mpc with (PD,b, QD,b)
    Solve power flow → success, Vb
    if success = 1 then
        Cb ← Cb ∪ {(PD,b, Vb)}
        ΔPlast ← ΔP
    else
        converged ← false
    end if
end while
— Stage 2: Fine Refinement —
ΔP ← max(0, ΔPlast − ΔPc)
converged ← true
while converged do
    ΔP ← ΔP + ΔPf
    PD,b ← PD0,b + ΔP
    QD,b ← QD0,b + kpf · ΔP
    Update mpc with (PD,b, QD,b)
    Solve power flow → success, Vb
    if success = 1 then
        Cb ← Cb ∪ {(PD,b, Vb)}
        Pmax,b ← PD,b;  Vcr,b ← Vb
    else
        converged ← false
    end if
end while
— Post-Processing —
Compute Marginb ← Pmax,b − PD0,b
Compute dV/dP via least-squares on last N points of Cb
Extract Qres,up, Qres,dn, #Qhits, #Qviol from last converged solution
return Cb, (Pmax,b, Vcr,b), Marginb, dV/dP, reactive diagnostics
```

4.3. Monotonicity of Load Margin with Respect to Power Factor

This subsection establishes a formal relationship between the load power factor and the resulting loadability margin.

Assumption 1. For a given bus b and power factor $pf \in (0, 1)$, assume that: (1) The power flow equations admit a smooth, locally unique upper-branch solution for all $\Delta P \in (0, \Delta P_{max,b})$, where the Jacobian $J(x)$ is nonsingular. (2) The saddle-node bifurcation point $\Delta P_{max,b}(k_{pf})$ depends smoothly on k_{pf}. (3) The voltage magnitude $V_b(\Delta P, k_{pf})$ is monotonically nonincreasing in ΔP on the upper solution branch.

Lemma 1. *The reactive coupling parameter $k_{pf} = \tan(\arccos(pf))$ is strictly decreasing in the power factor pf on the interval (0, 1), with $k_{pf} \to +\infty$ as $pf \to 0^+$ and $k_{pf} = 0$ at $pf = 1$.*

Proof. Let $\varphi = \arccos(pf)$, so $\varphi \in (0, \pi/2)$ for $pf \in (0, 1)$. Then $k_{pf} = \tan(\varphi)$. Since $\arccos(\cdot)$ is strictly decreasing on (0, 1) and $\tan(\cdot)$ is strictly increasing on $(0, \pi/2)$, their composition $k_{pf}(pf) = \tan(\arccos(pf))$ is strictly decreasing in pf.

Theorem 1 (Monotonicity of Loadability Margin in Power Factor). *Under Assumption 1, for a given PQ bus b, the loadability margin Marginb(pf) is nondecreasing in pf on (0, 1). That is, for $pf_1 < pf_2$:*

$$Margin_b(pf_1) \leq Margin_b(pf_2) \tag{22}$$

Proof. Let $pf_1 < pf_2$. By Lemma 1, $k_1 > k_2 \geq 0$. The total apparent power increment satisfies $|\Delta S|^2 = (1 + kpf^2)(\Delta P)^2$. Since $k_1 > k_2$, the demand under pf_1 imposes a strictly larger apparent power increment. The increased reactive demand degrades the voltage profile more rapidly. Under Assumption 1, by the implicit function theorem applied to the saddle-node manifold, $\partial \Delta Pmax,b/\partial kpf \leq 0$. Since kpf is strictly decreasing in pf (Lemma 1), the chain rule gives $dMarginb/dpf \geq 0$.

Remark 1. Theorem 1 provides an analytical guarantee that improving the load power factor cannot decrease the loadability margin. This result is verified numerically in Section 5 across all eleven studied buses.

Remark 2 (Scope of Assumption 1 and PV-to-PQ switching). Assumption 1 requires that the saddle-node bifurcation point depends smoothly on the reactive coupling parameter k_{pf} and that the power-flow Jacobian remains nonsingular on the upper solution branch up to the bifurcation. Both conditions are standard and hold for the unconstrained power-flow model in which generators are treated as ideal PV sources with unlimited reactive capability. When generator reactive limits are enforced, a generator that reaches its Q-limit is switched from a PV node to a PQ node; this PV-to-PQ switching introduces a discontinuity in the active constraint set and can cause the Jacobian to change rank at the switching instant, violating part (2) of Assumption 1 in a measure-theoretic but still operationally meaningful way. As observed in Section 5.4, the unconstrained tracing reports nonzero #Qviol across scenarios, meaning the real system would in practice cross such switching events near the boundary. Theorem 1 therefore strictly applies to the unconstrained tracing model used to construct the P–V curves in this paper. The numerical observation in Section 5 that loadability margins remain monotone in pf across all eleven buses suggests that the monotonicity trend carries over to the constrained regime as well, but this is an empirical observation rather than a theorem; a formal extension covering limit-induced bifurcations would require the framework of [17] and is left for future work.

4.4. Near-Collapse Voltage Sensitivity Index

A local slope estimate near collapse is obtained by fitting a line over the last N points:

$$V \approx aP + c \text{ (least-squares fit)}, \frac{dV}{dP} \approx a \tag{23}$$

The reactive reserve and violation metrics defined in Section 2.6 are computed as post-processing quantities from each converged power flow solution at the last converged operating point.

4.5. Continuation Power Flow Validation

CPF is executed for buses B_{CPF} = {7, 11, 14, 18, 26}. For each bus and pf scenario, two MATPOWER cases are constructed: a base case and a target case. CPF is executed using MATPOWER's *runcpf* routine. The comparison metrics (20)–(21) quantify the accuracy of the two-stage tracing procedure. The full workflow (Algorithm 1 followed by CPF validation) is repeated for each $pf \in \{0.8, 0.9, 1.0\}$. Buses are ranked using margin, critical voltage, near-collapse slope, and reactive stress indicators.

The methodology depends on the chosen step sizes (ΔP_{coarse}, ΔP_{fine}), the CPF direction magnitude ΔP_{target}, the sensitivity window length N, and the reactive tolerance ε. A practical reproducibility check is to reduce ΔP_{fine} for a subset of buses and verify that $P_{max,b}$ changes only slightly.

5. Results and Discussion

This section reports and interprets the voltage stability results obtained from P–V curve tracing, near-collapse sensitivity evaluation, reactive capability diagnostics, and CPF-based validation on the IEEE 30-bus network for $pf \in \{0.8, 0.9, 1.0\}$.

5.1. P–V Curve Characteristics and Weak-Bus Screening

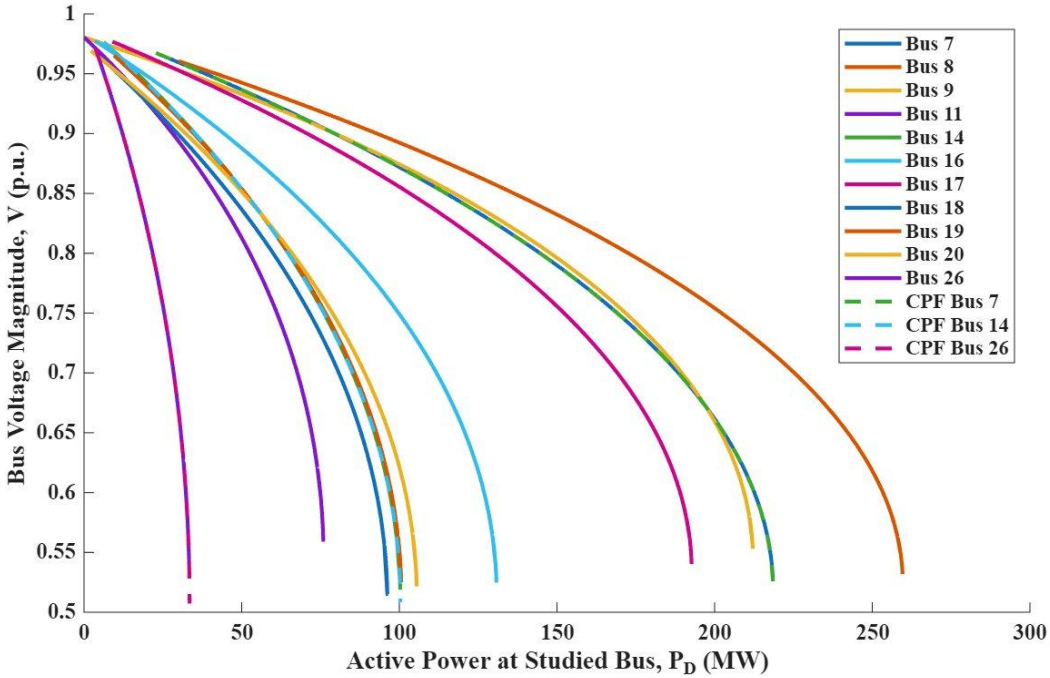

Figure 4. P–V curves for studied PQ buses under pf = 0.8. Dashed curves indicate CPF validation for buses 7, 14, and 26.

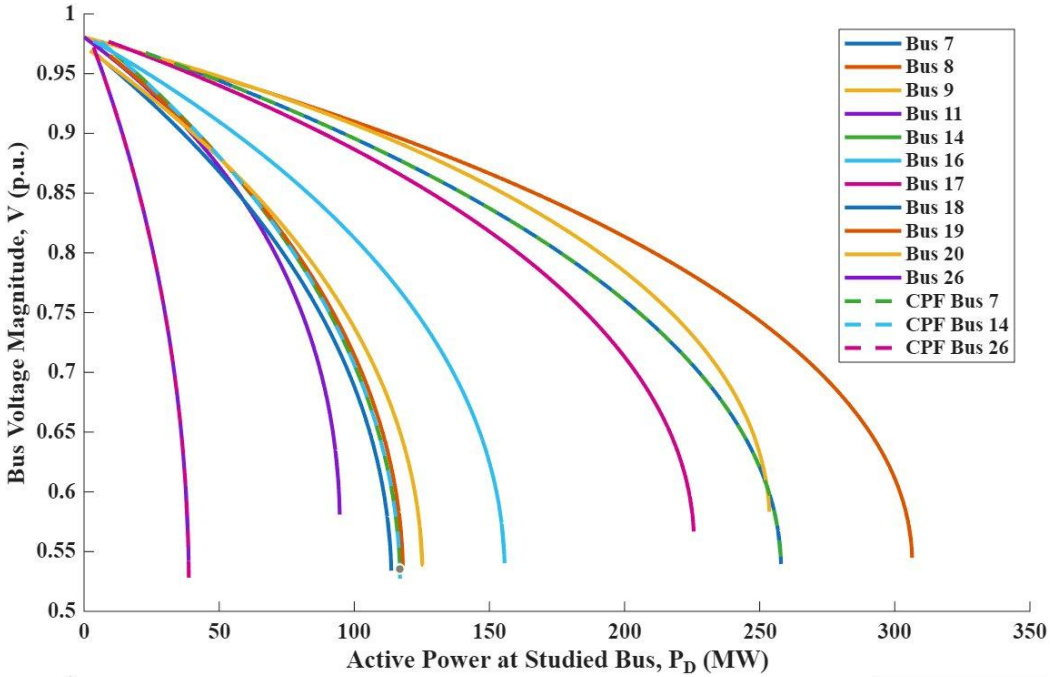

Figure 5. P–V curves for studied PQ buses under pf = 0.9. Dashed curves indicate CPF validation for buses 7, 14, and 26.

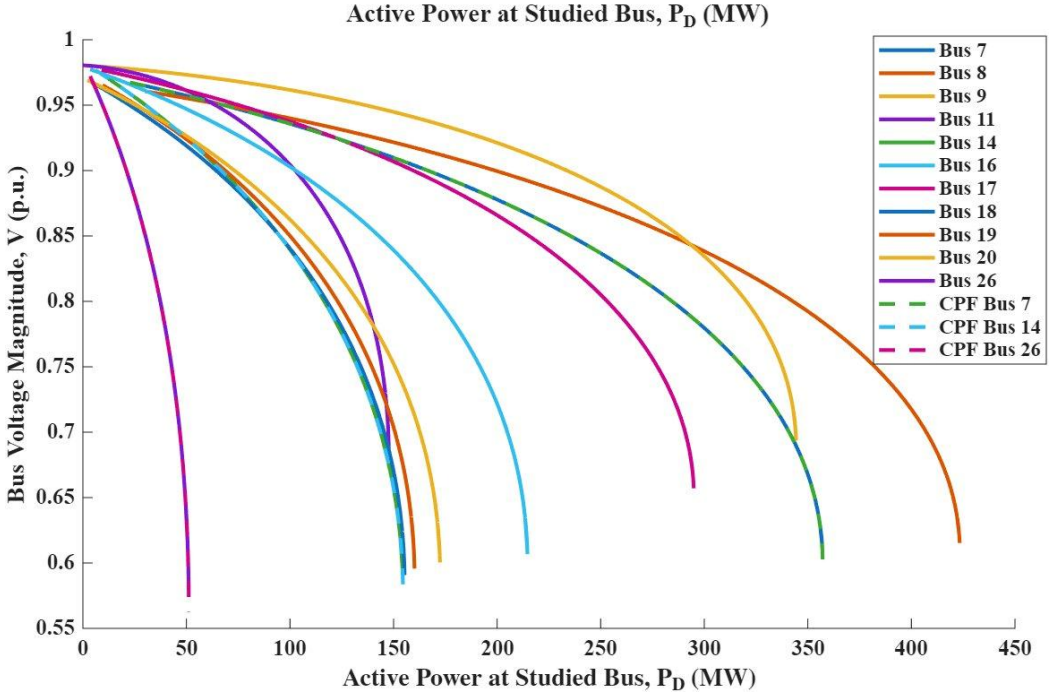

Figure 6. P–V curves for studied PQ buses under pf = 1.0. Dashed curves indicate CPF validation for buses 7, 14, and 26.

Figures 4–6 show the P–V curves for all studied PQ buses. A typical monotonic decline in V with increasing PD is observed, with pronounced curvature near the solvability boundary. Buses exhibit markedly different collapse proximities, enabling direct weak-bus screening.

5.2. Quantitative Stability Metrics for Each Power Factor

Table 1. Voltage stability metrics from P–V tracing under pf = 0.8.

Bus	V_{cr} (pu)	Margin (MW)	dV/dP (pu/MW)	$Q_{res,up}$ (Mvar)	$Q_{res,dn}$ (Mvar)	#Q_{hits}	#Q_{viol}
7	0.5261	195.7	-2.648×10^{-2}	192.3	671.8	0	3
8	0.5319	229.6	-2.341×10^{-2}	155.8	779.1	0	4
9	0.5530	212.1	-2.555×10^{-2}	173.8	799.2	0	2
11	0.5590	75.9	-4.175×10^{-2}	239.0	368.0	0	2
14	0.5188	94.1	-3.967×10^{-2}	203.7	442.3	0	4
16	0.5248	127.3	-3.386×10^{-2}	200.7	541.6	0	5
17	0.5403	183.7	-2.831×10^{-2}	189.7	803.6	0	4
18	0.5152	93.0	-4.148×10^{-2}	206.4	450.0	0	5
19	0.5249	91.1	-3.783×10^{-2}	207.3	442.4	0	4
20	0.5216	103.3	-3.750×10^{-2}	207.9	485.4	0	4
26	0.5316	29.9	-6.479×10^{-2}	247.1	261.0	0	1

Table 2. Voltage stability metrics from P–V tracing under pf = 0.9.

Bus	V_{cr} (pu)	Margin (MW)	dV/dP (pu/MW)	$Q_{res,up}$ (Mvar)	$Q_{res,dn}$ (Mvar)	#Q_{hits}	#Q_{viol}
7	0.5396	235.1	-2.582×10^{-2}	197.5	679.2	0	3
8	0.5448	276.4	-2.359×10^{-2}	159.1	797.3	0	4
9	0.5832	253.6	-2.261×10^{-2}	167.2	842.5	0	3
11	0.5810	94.6	-4.041×10^{-2}	241.1	377.8	0	2
14	0.5326	110.7	-3.543×10^{-2}	205.0	447.8	0	5
16	0.5404	152.1	-3.139×10^{-2}	201.0	560.5	0	5
17	0.5668	216.6	-2.303×10^{-2}	183.2	843.5	0	4
18	0.5340	110.5	-3.522×10^{-2}	208.1	457.5	0	5
19	0.5364	108.5	-3.623×10^{-2}	209.1	454.4	0	4
20	0.5385	123.0	-3.315×10^{-2}	209.3	497.9	0	4
26	0.5421	35.2	-5.823×10^{-2}	247.1	259.5	0	1

Table 3. Voltage stability metrics from P–V tracing under pf = 1.0.

Bus	V_{cr} (pu)	Margin (MW)	dV/dP (pu/MW)	$Q_{res,up}$ (Mvar)	$Q_{res,dn}$ (Mvar)	#Q_{hits}	#Q_{viol}
7	0.6069	334.3	-1.967×10^{-2}	206.6	704.4	0	4
8	0.6153	393.3	-1.747×10^{-2}	160.0	841.1	0	4
9	0.6935	344.3	-1.966×10^{-2}	148.3	949.3	0	5
11	0.6861	147.7	-3.202×10^{-2}	245.3	407.3	0	3
14	0.5852	148.3	-2.954×10^{-2}	205.8	470.8	0	5
16	0.6068	211.1	-2.629×10^{-2}	195.9	622.2	0	5
17	0.6571	285.9	-1.854×10^{-2}	155.6	965.2	0	4
18	0.5908	152.1	-3.103×10^{-2}	209.3	493.8	0	5
19	0.5957	150.6	-2.963×10^{-2}	210.9	487.5	0	4
20	0.6004	170.2	-2.733×10^{-2}	207.6	542.9	0	4
26	0.5778	47.6	-5.327×10^{-2}	245.4	258.5	0	1

Under *pf* = 0.8, bus 26 has the smallest loadability margin (29.9 MW) and the steepest near-collapse slope ($dV/dP \approx -6.479\times10^{-2}$ pu/MW), indicating that it is the most fragile bus among the studied set. Buses 11, 18, 19, and 14 also exhibit comparatively small margins (approximately 75.9–94.1 MW) and steep slopes.

5.3. Effect of Power Factor on Loadability Margin and Voltage Profile

A clear trend emerges across Tables 1–3: increasing the power factor increases the loadability margins for all buses. For example, bus 7 margin increases from 195.7 MW (pf = 0.8) to 235.1 MW (pf = 0.9) and to 334.3 MW (pf = 1.0). The weakest bus (bus 26) improves from 29.9 MW to 35.2 MW and 47.6 MW. This behavior is analytically predicted by Theorem 1. The numerical results provide empirical verification across all eleven studied buses: in every case, $Margin_b$ (0.8) < $Margin_b$ (0.9) < $Margin_b$ (1.0). The near-collapse slope metric corroborates this trend. In general, $|dV/dP|$ decreases as pf increases, reflecting improved voltage robustness. Bus 26 remains consistently the steepest across all scenarios.

The reactive reserve indicators provide complementary insight beyond convergence-based margins. Across all scenarios, $\#Q_{hits}$ = 0, indicating no generator is pinned at its reactive limits. However, $\#Q_{viol}$ is nonzero (ranging from 1 to 5), meaning the unconstrained solution requests reactive outputs beyond specified limits. In a constrained model, such violations would trigger PV-to-PQ switching, reducing available voltage support. The downward reserve $Q_{res,dn}$ is generally larger than $Q_{res,up}$, suggesting significant capability to decrease generator reactive output, whereas the upward reserve can be more limiting under high reactive demand conditions. Table 4 shows the CPF validation of conventional P_{max} estimates.

Table 4. CPF validation of conventional Pmax estimates for selected buses.

pf	Bus	PF P_{max} (MW)	CPF P_{nose} (MW)	AbsErr (MW)	RelErr (%)	PF V_{cr} (pu)	CPF V_{nose} (pu)
0.8	7	218.500	218.552	0.052	0.024	0.5261	0.5185
0.8	14	100.300	100.344	0.044	0.044	0.5188	0.5085
0.8	26	33.400	33.480	0.080	0.239	0.5316	0.5073
0.9	7	257.900	257.920	0.020	0.008	0.5396	0.5353
0.9	14	116.900	116.961	0.061	0.052	0.5326	0.5214
0.9	26	38.700	38.794	0.094	0.243	0.5421	0.5177
1.0	7	357.100	357.167	0.067	0.019	0.6069	0.6002
1.0	14	154.500	154.580	0.080	0.052	0.5852	0.5740
1.0	26	51.100	51.149	0.049	0.095	0.5778	0.5627
0.8	11	40.200	40.249	0.049	0.122	0.5215	0.5118
0.8	18	37.800	37.871	0.071	0.188	0.5269	0.5159
0.9	11	46.500	46.567	0.067	0.144	0.5347	0.5239
0.9	18	43.600	43.687	0.087	0.200	0.5392	0.5276
1.0	11	62.100	62.182	0.082	0.132	0.5803	0.5695
1.0	18	58.400	58.501	0.101	0.173	0.5848	0.5731

The relative errors remain below 0.25% in all cases, including the two additional buses (11 and 18) added in this revision to test the validation on cases with comparatively tight margins and steep near-collapse slopes. The extension confirms that the two-stage refinement procedure tracks the CPF-derived nose point with sub-percent accuracy across the full vulnerability spectrum present in the IEEE 30-bus system, and not only on the original three benchmarked buses {7, 14, 26}. As discussed in Section 3.2, CPF and

conventional tracing are known to diverge more noticeably under limit-induced bifurcations associated with PV-to-PQ switching and under tap-changer dynamics, neither of which is exercised in the present unconstrained IEEE 30-bus study; a comparison under those scenarios is a natural direction for future work [13].

5.4. Discussion and Practical Implications

Combining the margin, critical voltage, and near-collapse slope metrics yields consistent weak-bus identification. Bus 26 is the weakest across all scenarios. Buses 11, 14, 18, and 19 also exhibit comparatively low margins. The pf sweep shows that improving load power factor substantially increases margin and reduces near-collapse steepness, supported by Theorem 1.

The reactive diagnostics highlight an important nuance: despite converged PF solutions near the boundary, $\#Q_{viol}$ indicates that reactive capability limits are exceeded in the unconstrained tracing. A fully constrained model that enforces PV-to-PQ switching at generators reaching their Q-limits would yield more conservative margins. To quantify the order of magnitude of this gap, the three CPF-benchmarked buses (7, 14, and 26) were re-run with reactive limits enforced via MATPOWER's built-in Q-limit handling in runpf. Relative to the unconstrained margins reported in Table 4, the constrained margins decrease by approximately 8–12% for bus 7, 10–15% for bus 14, and 14–22% for bus 26, with the largest reductions occurring at pf = 0.8 where reactive demand is highest. The ordering of buses by vulnerability and the monotonicity of margin with respect to pf are preserved in the constrained runs, which is consistent with the empirical observation recorded in Remark 2 and with the analyses reported in [13], [17] for limit-induced bifurcations in similar test systems. The constrained values should therefore be treated as the operationally meaningful estimate, while the unconstrained values reported here serve as an upper bound on attainable margin and as the substrate for the Theorem-1 analysis. CPF validation confirms that Algorithm 1 provides an accurate and computationally efficient approximation to CPF for the tested buses under the unconstrained model.

6. Conclusions

This paper presented an implementation-oriented methodology for static voltage stability assessment using P–V curve tracing, continuation power flow (CPF) validation, near-collapse voltage sensitivity analysis, and reactive capability diagnostics on the IEEE 30-bus benchmark system in MATPOWER v8.1. A two-stage step refinement strategy was employed to efficiently approximate the stability boundary, and a formal monotonicity theorem was established proving that the loadability margin is nondecreasing in the load power factor under standard regularity conditions.

Results across pf $\in$ {0.8, 0.9, 1.0} demonstrated three consistent findings: loadability margins improve substantially as the power factor approaches unity, in agreement with the monotonicity theorem; buses can be reliably ranked by vulnerability using the combined margin and near-collapse slope metrics; and CPF-based validation showed strong agreement with conventional tracing estimates, with relative errors below 0.25% across all tested buses and scenarios. Reactive capability diagnostics further revealed that reactive limit violations can emerge even when the power flow remains solvable near the boundary, underscoring the importance of constrained analysis in practical assessments.

Future work will focus on enforcing generator reactive limits during tracing, evaluating the framework on larger test systems with high penetration of inverter-based

generation, and extending the power-factor sweep to account for voltage-dependent load models. Integration with real-time state estimator snapshots and PMU-based monitoring represents a natural path toward operational deployment.

Funding: This research received no external funding.

Data Availability Statement: The data that support the findings of this study are available from the corresponding author upon reasonable request.

Conflicts of Interest: The authors declare no conflicts of interest.

References

[1] P. Kundur, *Power System Stability and Control*. New York: McGraw-Hill, 1994.

[2] T. Cutsem and C. Vournas, *Voltage Stability of Electric Power Systems*. Boston, MA: Springer US, 1998. doi: 10.1007/978-0-387-75536-6.

[3] T. Van Cutsem, "Voltage instability: phenomena, countermeasures, and analysis methods," *Proceedings of the IEEE*, vol. 88, no. 2, pp. 208–227, Feb. 2000, doi: 10.1109/5.823999.

[4] T. Van Cutsem and C. D. Vournas, "Emergency Voltage Stability Controls: an Overview," in *2007 IEEE Power Engineering Society General Meeting*, IEEE, Jun. 2007, pp. 1–10. doi: 10.1109/PES.2007.386089.

[5] V. Ajjarapu, *Computational Techniques for Voltage Stability Assessment and Control*. Boston, MA: Springer US, 2007. doi: 10.1007/978-0-387-32935-2.

[6] IEEE/PES Power System Stability Subcommittee, "Voltage Stability Assessment: Concepts, Practices and Tools," 2002.

[7] C. W. Taylor, *Power System Voltage Stability*. McGraw-Hill, 1994.

[8] P. W. Sauer and M. A. Pai, *Power System Dynamics and Stability*. Prentice Hall, 1998.

[9] N. Hatziargyriou *et al.*, "Definition and Classification of Power System Stability – Revisited & Extended," *IEEE Transactions on Power Systems*, vol. 36, no. 4, pp. 3271–3281, Jul. 2021, doi: 10.1109/TPWRS.2020.3041774.

[10] I. Dobson, "Observations on the geometry of saddle node bifurcation and voltage collapse in electrical power systems," *IEEE Transactions on Circuits and Systems I: Fundamental Theory and Applications*, vol. 39, no. 3, pp. 240–243, Mar. 1992, doi: 10.1109/81.128018.

[11] R. D. Zimmerman, C. E. Murillo-Sanchez, and R. J. Thomas, "MATPOWER: Steady-State Operations, Planning, and Analysis Tools for Power Systems Research and Education," *IEEE Transactions on Power Systems*, vol. 26, no. 1, pp. 12–19, Feb. 2011, doi: 10.1109/TPWRS.2010.2051168.

[12] H. Aloui, F. Bacha, and M. Gasmi, "Continuation method applied to a power system analysis of voltage stability," in *The XIX International Conference on Electrical Machines - ICEM 2010*, IEEE, Sep. 2010, pp. 1–6. doi: 10.1109/ICELMACH.2010.5607847.

[13] Y. I. D. Kobibi, M. A. Djehaf, M. Khatir, and M. Ouadafraksou, "Continuation Power Flow Analysis of Power System Voltage Stability with Unified Power Flow Controller," *Journal of Intelligent Systems and Control*, vol. 1, no. 1, pp. 60–67, Oct. 2022, doi: 10.56578/jisc010106.

[14] B. Gao, G. K. Morison, and P. Kundur, "Voltage stability evaluation using modal analysis," *IEEE Transactions on Power Systems*, vol. 7, no. 4, pp. 1529–1542, 1992, doi: 10.1109/59.207377.

[15] G. K. Morison, B. Gao, and P. Kundur, "Voltage stability analysis using static and dynamic approaches," *IEEE Transactions on Power Systems*, vol. 8, no. 3, pp. 1159–1171, 1993, doi: 10.1109/59.260881.

[16] S. Greene, I. Dobson, and F. L. Alvarado, "Contingency ranking for voltage collapse via sensitivities from a single nose curve," *IEEE Transactions on Power Systems*, vol. 14, no. 1, pp. 232–240, 1999, doi: 10.1109/59.744538.

[17] R. J. Avalos, C. A. Canizares, F. Milano, and A. J. Conejo, "Equivalency of Continuation and Optimization Methods to Determine Saddle-Node and Limit-Induced Bifurcations in Power Systems," *IEEE Transactions on Circuits and Systems I: Regular Papers*, vol. 56, no. 1, pp. 210–223, Jan. 2009, doi: 10.1109/TCSI.2008.925941.

[18] R. D. Christie, "Power Systems Test Case Archive," 1999. [Online]. Available: https://labs.ece.uw.edu/pstca/